

A three dimensional regional modeling study of the impact of clouds on sulfate distributions during TRACE-P

C. Kittaka,¹ R. B. Pierce,² J. H. Crawford,² M. H. Hitchman,³ D. R.
Johnson,³ G. J. Tripoli,³ M. Chin,⁴ A. R. Bandy,⁵ R. J. Weber,⁶ R. W.
Talbot⁷ and B. E. Anderson²

¹Science Applications International
Corporation, Hampton, VA, USA

²NASA Langley Research Center, Hampton,
VA, USA.

³Department of Atmospheric and Oceanic
Sciences, University of Wisconsin, Madison,
WI, USA

⁴NASA Goddard Space Flight Center,
Greenbelt, MD, USA

⁵Department of Chemistry, Drexel
University, Philadelphia, PA, USA.

⁶School of Earth and Atmospheric Sciences,
Georgia Institute of Technology, Atlanta, GA,
USA

⁷Institute for the Study of Earth, Oceans
and Space, University of New Hampshire,
Durham, NH, USA

Abstract.

The University of Wisconsin Nonhydrostatic Modeling System (UWNMS) is combined with an aqueous sulfur chemistry module to simulate the sulfate transport in East Asia during the TRACE-P period. Lateral boundary conditions for the regional simulations were obtained from the Global Ozone Chemistry Aerosol Radiation and Transport (GOCART) and Regional Air Quality Modeling System (RAQMS) models. The simulated results are compared with in-situ and satellite measurements collected during the TRACE-P period. Volume integrated sulfate mass in the model domain is calculated. Significant amounts of sulfate (volume integrated mass: $1.5 \times 10^6 - 7.5 \times 10^6 kg$) are released into air after being produced in clouds through the oxidation of sulfur dioxide by hydrogen peroxide. Instantaneous sulfate mass within clouds varies from $0.2 \times 10^6 kg$ to $3.5 \times 10^6 kg$. Sulfate mass removed through precipitation is in the ranges between $0.01 \times 10^6 kg$ and $1.8 \times 10^6 kg$. This study shows that the sulfate input to the atmosphere exceeds the sulfate removed from the atmosphere through precipitation in the East Asian region during the TRACE-P. Consequently, East Asia in spring can be an important source region of sulfate and thus offset the sulfate loss through precipitation scavenging in other regions of the globe.

1. Introduction

There has been significant progress in understanding aerosol composition and distributions in the troposphere during the last 20 years. This was in response to strong demands for: 1) assessing the aerosol effects on the earth radiative balance [e.g. IPCC, 2001], 2) reducing air pollution associated with aerosol particles. One important key to this progress is the global coverage provided by satellite observations at high spatial resolution from instruments such as the Moderate-Resolution Imaging Spectroradiometer (MODIS) and the Multi-angle Imaging SpectroRadiometer (MISR). These observations allow us to monitor global aerosol distributions and to diagnose aerosol loadings in a retrospective fashion. For predicting and assimilating aerosol fields, several models have been developed with different representations of chemical composition, particle size distributions, chemical processes in both gas and aqueous phases, and interactions between aerosol particles and also between cloud drops (liquid and ice) and aerosol particles.

One of major constituents of aerosol is sulfate. Sulfate is produced predominantly via the oxidation of sulfur species (sulfur dioxide (SO_2), dimethyl sulfide (DMS), hydrogen sulfide (H_2S) and carbonyl sulfide (OCS)) in the atmosphere. Sulfur dioxide is a major precursor of sulfate in a tropospheric polluted environment. SO_2 is oxidized to sulfate mainly by hydroxyl radical in the gas phase while it is oxidized mainly by hydrogen peroxide (H_2O_2), ozone (O_3) or with iron ($Fe(III)$) through catalyzed reactions in the aqueous phase [Seinfeld and Pandis, 1998; Kreidenweis et al., 1997]. It has been found that the SO_2 oxidation rate in the gas phase is much slower than that in the aqueous phase, i.e. 5% per hour in the gas phase and several hundred percent per hour (an equivalent gas-phase rate of SO_2 conversion to sulfate) in the aqueous phase [Calvert et al., 1985]. Of

the three major oxidation pathways in the aqueous phase, hydrogen peroxide is found to be the most effective oxidant under SO_2 abundant conditions [Kreidenweis et al., 1997]. Clouds play a major role in the formation and re-distribution of sulfate both locally and globally by providing a unique environment where liquid drops and ice crystals provide an effective medium for chemical reactions and cloud dynamical evolution provides a means for rapid vertical transport of chemical substances [e.g., Dickerson et al., 1987; Pickering et al., 1996].

Sulfate in-cloud production not only adds sulfate mass to the local atmosphere but can also modify the aerosol size distribution. Observations show that populations of aerosol particles that have been processed in clouds have a distinct peak at $0.1 - 1\mu m$ diameter range in the size distribution [e.g. Hoppel et al., 1990]. The suggested mechanism for creating this peak in aerosol size distribution is the following. Cloud drops nucleate on cloud condensation nuclei (CCN). As the cloud evolves, the cloud drops absorb water-soluble chemical species, adding mass to the existing chemical species in the drops. When the cloud evaporates, the chemical species may be released as aerosol particles, which are larger in size than the original CCN. In case of SO_2 and H_2O_2 scavenging by clouds, SO_2 may be oxidized by H_2O_2 to produce sulfate. Consequently, aerosol particles processed in clouds have increased sulfate mass and produce an additional peak in the size distribution. Adding sulfate mass to CCN considerably alters the physicochemical and optical properties of CCN by enhancing the hygroscopy of aerosol particles. This leads to the modification of cloud properties and rain persistence, thereby affecting the local radiative and hydrological balance.

East Asia is one of largest source regions of sulfur dioxide in the world, although sulfur oxide emissions have decreased in recent years due to the slowdown of East Asian economic development [Streets et al., 2003]. Air masses influenced by these emissions may travel long distances due to the strong westerlies within the Japan jet stream during spring. There is evidence that the East Asian outflow modifies the air mass characteristics downwind and adversely affects the North Pacific and North American air quality [Jaeglé et al., 2003; Price et al., 2003]. As one of the NASA Global Tropospheric Experiment (GTE) efforts, Transport and Chemical Evolution over the Pacific (TRACE-P) was conducted in spring 2001 to characterize the Asian chemical outflow and to determine its chemical evolution [Jacob et al., 2003]. Tu et al. [2003] describe the SO_2 distributions measured during the TRACE-P period under different meteorological conditions. SO_2 concentrations appeared to be influenced (reduced) by clouds during the TRACE-P flights. Tu et al. [2003] compared model results obtained from CFORS/STEM-2K1 [Carmichael, 2003] with the measured concentrations. The comparisons showed the model poorly represented the SO_2 distributions for the cloudy cases whereas the modeled SO_2 distributions were in good agreement with the measured values for a clear sky cases. Crawford et al. [2003] also found the observational evidence for cloud scavenging of SO_2 and HNO_3 during the TRACE-P period.

The objective of this paper is to estimate the sulfate production via in-cloud processing in East Asia during the TRACE-P period using the UWNMS (University of Wisconsin Nonhydrostatic Modeling System). UWNMS forms the dynamical core of the regional component of Regional Air Quality Modeling System (RAQMS). RAQMS was used to estimate the tropospheric ozone budget over East Asia during the TRACE-P period [Pierce

et al., 2003], also the carbon monoxide transport for the TRACE-P period [Kiley et al., 2003]. A companion paper by Hitchman et al. [2003] also uses the UWNMS to discuss the TRACE-P flight of March 24 with a focus on transport of alcohols and stratospheric ozone by the convectively induced circulation. For this study, the UWNMS is coupled with an aqueous sulfur chemistry model, which represents the oxidation of SO_2 by H_2O_2 in the aqueous phase. Other competing processes in sulfate production such as gas phase reactions and the oxidation of other sulfur species are considered to be of secondary importance for sulfate in-cloud production and not included in the model. Two global models provide initial and lateral boundary conditions for the regional model simulations. The global component of RAQMS [Pierce et al., 2003] provides H_2O_2 distributions for the boundary conditions of the regional model. Because *RAQMS* does not employ sulfur chemistry, the Global Ozone Chemistry Aerosol Radiation and Transport (GOCART) model [Chin et al., 2000a, 2000b, 2002, 2003] is used for SO_2 and sulfate boundary conditions of the regional model.

In the following section the components of models used are briefly described. In Section 3 we characterize the regional model performance of predicting the atmospheric components involved in the sulfate in-cloud production, such as the distributions of SO_2 , sulfate, H_2O_2 , liquid water in clouds, and precipitation by comparing these components with TRACE-P aircraft measurements and satellite observations. We then describe a case study for March 24, 2001, when the air influenced by a deep convective storm was advected from the east coast of China to the south of the Japan islands (Section 4). We conclude by estimating the contribution of the sulfate in-cloud production to the sulfate budget for the TRACE-P period (Section 5).

2. Regional model description

2.1. The meteorological model

The regional meteorological model is University of Wisconsin Nonhydrostatic Modeling System (UWNMS) developed by Tripoli [1992]. UWNMS is a three-dimensional nonhydrostatic mesoscale model which uses the quasi-compressible approximation. It has been used for operational mesoscale weather forecasts in the University of Wisconsin-Madison (<http://mocha.meteor.wisc.edu/>). For this study, five water categories, total moisture, water vapor, rain, ice crystal and snow, are carried as separate prognostic variables. Specific mass of total moisture is defined as:

$$q_t = q_v + q_c + q_r + q_i + q_s \quad (1)$$

where $q_t, q_v, q_c, q_r, q_i, q_s$ is specific mass of total moisture, water vapor, cloud water, rain, ice crystal and snow, respectively. Liquid cloud water (q_c) is diagnosed using specific masses of the other five water categories. The reader is referred to Tripoli [1992] for a complete description of the physical parameterizations used to simulate cloud physics, the surface layer, radiative process and subgrid scale moist convection. An aqueous sulfur chemistry model is incorporated into UWNMS for this study as follows.

2.2. Aqueous sulfur chemistry

An aqueous sulfur chemistry model is used to represent the sulfate production in water clouds and subsequent re-distribution of sulfate into different water categories due to the cloud microphysical transformation [Kittaka, 2001]. The chemical species included in the model are SO_2 and H_2O_2 in the gas phase, $S(IV)$ (SO_2 and bisulfide (HSO_3^-)), $S(VI)$ (HSO_4^- and SO_4^{2-}), and H_2O_2 in the aqueous phase, and $S(VI)$ in the aerosol phase. Additionally the association of these species with different hydrometeors, such

as cloud water, rain water, ice crystal and snow, is explicitly predicted in accordance with the cloud microphysical transformation. The primary chemical reaction of the sulfur chemistry model is the oxidation of SO_2 by H_2O_2 . This is the most dominant reaction under cloudy and polluted conditions in the troposphere [Seinfeld and Pandis, 1998].

The chemical equations are:



The production rate of sulfate is given as:

$$\frac{d[S(VI)]}{dt} = \frac{\kappa_{oxi}[H^+][H_2O_2][HSO_3^-]}{1 + K[H^+]} \quad (7)$$

where κ_{oxi} is the rate constant and $\kappa_{oxi} = 7.5 \times 10^7 M^{-1} s^{-1}$ and $K = 13 M^{-1}$ at 298K [Seinfeld and Pandis, 1998]. Because $(1 + K[H^+]) \simeq 1$ in the atmospheric environment, the equation above can be simplified as:

$$\frac{d[S(VI)]}{dt} = \kappa_{oxi}[H^+][H_2O_2][HSO_3^-] \quad (8)$$

The temperature dependence of the oxidation rate constant is given as:

$$\kappa_{oxi}(T) = \kappa_{oxi}(298) \exp\left(\frac{\Delta H}{R} \left(\frac{1}{298} - \frac{1}{T}\right)\right) \quad (9)$$

where $\frac{\Delta H}{R} = -4430K$ [Seinfeld and Pandis, 1998].

The sulfate production rate is a function of the concentrations of H_2O_2 , H^+ and HSO_3^- . The concentration of HSO_3^- in turn is a function of H^+ as the equation 3 shows. The

following assumptions are used to construct the aqueous sulfur chemistry model. 1) Only a liquid water drop such as a cloud water drop and a rain drop may directly interact with chemical species. This is a reasonable assumption since laboratory studies have shown that under atmospheric conditions the direct gas uptake by ice crystals may be neglected in comparison to the uptake of gases by water drops [Diehl et al., 1998]. 2) Gases may be absorbed into water drops and subsequently get incorporated into ice through the riming process [Diehl et al., 1998; Borys et al., 1988; Mitchell and Lamb, 1989]. This process is included in the model cloud microphysical transformation. 3) The chemical species are in equilibrium between the gas phase and liquid phase regardless of drop size. Schwartz [1988] found that interfacial mass transport of H_2O_2 and SO_2 is not a limitation to the in-cloud reaction under conditions of interest and this rules out any drop-size dependence to the kinetics of the reaction. Thus, the Henry's law approximation may be applied to determine the concentrations of the chemical species in the aqueous phase. 4) Ambient carbon dioxide (CO_2) with a mixing ratio of 300ppm is assumed in order to slightly acidify water drops to $pH \simeq 5.6$ before any other chemical reactions take place. This CO_2 mixing ratio remains constant throughout a model run. 5) Sulfate released into air after being produced in clouds is assumed to be in the aerosol phase.

The continuity equation of a chemical substance C is given as

$$\frac{d[C_i]}{dt} = \left(\frac{d[C_i]}{dt} \right)_{ABS} + \left(\frac{d[C_i]}{dt} \right)_{CHEM} + \left(\frac{d[C_i]}{dt} \right)_{MP} \quad (10)$$

where C_i represents the concentration of a chemical substance C associated with a water category (or air) i . C may be $S(IV)$, $S(VI)$ or H_2O_2 whereas the subscript (i) may be a (air), t (total cloud water including water in the liquid and ice phases), r (rain drop), i (ice crystal), or s (snow). $S(VI)_a$ is sulfate suspended in air and considered to be in the

aerosol phase (see the assumption 5 above). Sulfate within liquid cloud water $S(VI)_c$ is diagnosed using $S(VI)_t$, $S(VI)_r$, $S(VI)_i$, and $S(VI)_s$. The first term on the right hand side represents the change due to the absorption of chemical substance C into cloud water or rain. The second term is the change due to chemical reactions listed above. The last term represents the change due to cloud microphysical transformation. The removal of chemical species through rain out is also included in this term. SO_2 dry deposition, which accounts for a SO_2 removal pathway of about 30% of global SO_2 emissions [Davis et al., 2003], is not included in the model. This is expected to introduce a high bias in simulated SO_2 mixing ratios.

In order to quantify the in-cloud production of sulfate, we consider two sulfate variables. One is an idealized sulfate tracer, which is subject only to advection and mixing, hereafter $S(VI)_{trc}$. The other is sulfate in air, $S(VI)_a$ as defined above, which has been subject to in-cloud processing and precipitation in addition to advection and mixing. The difference between these two sulfates accounts for sulfate released into air after being produced in clouds.

2.3. Boundary conditions

In order to incorporate H_2O_2 variability associated with global meteorological conditions, the global H_2O_2 fields were obtained from *RAQMS* and used as boundary conditions for the regional H_2O_2 distribution.

GOCART [Chin et al., 2000a, 2000b, 2002, 2003] is used to initial and lateral boundary conditions for the regional sulfate and SO_2 predictions. GOCART primarily predicts global aerosol distributions of sulfate, dust, organic carbon (OC), black carbon (BC) and sea-salt using assimilated meteorological fields from the Goddard Earth Observing System

Data Assimilation System (GEOS DAS). The sulfur species included are SO_2 , sulfate, dimethylsulfide (DMS), and methanesulfonic acid (MSA). SO_2 and DMS are subject to oxidation by prescribed oxidants (OH , NO_3 and H_2O_2 from Muller and Brasseur [1995]). For lateral boundary conditions the 6 hourly global sulfate and SO_2 distributions (GOCART $2^\circ \times 2.5^\circ$, latitude/longitude resolution) and global H_2O_2 distribution (RAQMS $2^\circ \times 2^\circ$, resolution) results are interpolated to every time step of the regional model run and imported to adjust the outer three grid points of the regional model domain. This gives chemical constraints to the regional fields. This is particularly important for SO_2 and sulfate because the large portion of sulfur sources are located further west of the regional model domain and the sulfur species emitted from the region are known to be advected eastward.

3. TRACE-P simulation

A simulation of the sulfate transport between March 7 and April 3, 2001 in East Asia was conducted. The domain of the regional model included the eastern half of China, the Korean Peninsula, the southeast Russia, the Japan islands and the northwestern Pacific (see Fig 6). The model domain extended vertically up to $20km$. The spatial resolution of the regional model was $110km$ and $0.4km$ horizontally and vertically, respectively, and the integration time step was 3 minutes. 6 hour meteorological fields from the NOAA National Centers for Environmental Prediction (NCEP) Aviation Model (AVN) $1^\circ \times 1^\circ$ analysis were used for lateral meteorological boundary conditions. Potential temperature and water vapor predictions in the UWNMS model were relaxed toward the NCEP-AVN assimilated fields to give weak meteorological constraints to the regional fields. The 1° gridded SO_2 anthropogenic emissions from the 2000 inventory constructed by Streets

[2003] were used. The SO_4 emissions are an order of magnitude smaller than those of SO_2 [Davis et al., 2003] therefore not included here.

4. Results

4.1. Comparisons with measurements

4.1.1. Sulfate, sulfur dioxide and hydrogen peroxide.

Fig 1(a)-(c) show comparisons of SO_2 , sulfate and H_2O_2 mixing ratios at five different altitude ranges between measured and simulated values for all flights (ten DC-8 flights and ten P-3B flights for SO_2 and sulfate, ten DC-8 flights for H_2O_2) from March 7 to April 3, 2001. Fine aerosol non-sea-salt sulfate ($nss\ SO_4$) measurements using mist chamber ion chromatography on DC-8 [Dibb, 2003] and sulfate as aerosol bulk ionic composition measurements using PILS-Ion chromatography on P-3B [Weber, 2003] are used and compared with the predicted sulfate $S(VI)_a$. It should be noted that SO_2 mixing ratios measured on P-3B flights are found to be higher than those on DC-8 according to the intercomparison studies [Eisele et al., 2003]. The simulated values are sampled along the flight tracks. The figures illustrate a monotonic decrease of the mixing ratios of these three species with altitude. At all altitudes the model overestimates sulfur dioxide mixing ratio by a factor of 1.2-3. This is probably due to a lack of SO_2 dry deposition in the model. The observed variability of sulfur dioxide below $2km$ is much larger than the simulated variability. This may be due to the annual average SO_2 emission rate used in the simulation and the neglect of ocean DMS emissions. Sulfate is underestimated near the ground and in the upper troposphere whereas it is overestimated by a factor of 1.2 between $1km-6km$. Hydrogen peroxide is overestimated by a factor of 1.2-2 at all altitude ranges except between $1km$ and $4km$, where the simulation results are in good agreement

with the measured mixing ratios. The overestimate is larger at higher altitudes. The combination of the overestimate of sulfur dioxide and the underestimate of sulfate in the boundary layer suggests either lower conversion rates of sulfur dioxide to sulfate or lower liquid water mixing ratio in the model.

Comparisons at six different latitude ranges are shown in Fig 2(a)-(c). It should be noted that intensive volcanic activity was observed at Miyake-jima ($34.08^{\circ}N$, $139.53^{\circ}E$), where a significant amount of SO_2 was emitted into the low troposphere during the TRACEP period. This volcanic emission was not included in the model simulation. The elevated SO_2 mixing ratios ($\sim 10ppbv$) sampled in the southeast of Japan on P-3B Flt.14 (March 18) and Flt.17 (March 27) were suggested to be directly affected by this volcanic activity according to the mission summary for that flight. Relatively high mixing ratios of SO_2 and sulfate are seen at $27.5^{\circ}N - 42.5^{\circ}N$ whereas high H_2O_2 mixing ratios are found at lower latitudes ($\leq 27.5^{\circ}N$). The H_2O_2 mixing ratios at $35^{\circ}N$ are slightly lower than those at the adjacent latitude ranges. This may attribute to the absorption of H_2O_2 into liquid water, which is slightly enhanced at $35^{\circ}N$ (not shown).

4.1.2. Cloud and rain fields.

It is challenging to accurately predict cloud water and precipitation. During in-cloud processing, cloud water acts as a medium for chemical reactions and also provides pathways for chemical substances to get incorporated into ice phase. Precipitation is a removal process for chemical substances with large solubilities such as SO_2 , sulfate and H_2O_2 . To evaluate the UWNMS cloud prediction we compare the predicted vertically integrated liquid water path (LWP) with that derived from the data obtained from the Moderate-Resolution Imaging Spectroradiometer (MODIS) instrument onboard the Terra platform.

The MODIS LWP data sets ($15^{\circ}N - 50^{\circ}N$ and $115^{\circ}E - 150^{\circ}E$) used here are taken from the Level-3 Atmospheric Daily Global Product ($1^{\circ} \times 1^{\circ}$ cells on an equal-angle grid). 0Z UWNMS LWP predictions, which are closest to MODIS (Terra) overpass, are used in the comparison. Both data sets are sorted into 35 latitudinal bins between $15^{\circ}N$ and $50^{\circ}N$ with 1° spacing. Fig 3(a) shows the comparison of the latitudinal variation of LWP between UWNMS and MODIS for the simulation period. LWP of more than $20g/m^2$ is considered to effectively contribute to the sulfate in-cloud production and is used in the comparisons. The number of sample points considered varies from 20 to 330. Median, upper and lower 90 percentiles of LWP ($\geq 20g/m^2$) are shown. Both UWNMS and MODIS LWP are highly variable with latitude. The peaks at $\sim 21^{\circ}N$ in the UWNMS LWP curves are not observed. This is, however, statistically insignificant because there are few predicted points in this latitude range. Except for the lower latitudes, UWNMS generally captures the latitudinal variation of LWP. The fraction of LWP exceeding $20g/m^2$ in the domain is plotted as a function of latitude in Fig 3(b). This comparison clearly indicates that the UWNMS liquid water is distributed in a more confined area ($25^{\circ}N - 32^{\circ}N$) than MODIS LWP, which shows a broader spread in latitude. The underestimate in the predicted liquid water frequency south of $24^{\circ}N$ may be due to a lack of explicit inflow of liquid water through the model boundaries. In the simulated atmosphere most clouds in the north of $40^{\circ}N$ are in the ice phase. Despite these discrepancies, both UWNMS and MODIS LWP clearly show the storms passing at about $28^{\circ}N$ during the simulation period.

UWNMS daily precipitation was calculated using 12-hour accumulated precipitation. Latitudinally binned UWNMS daily precipitation is compared with precipitation esti-

mates based on the Tropical Rainfall Measuring Mission (TRMM) data (available up to 40°) [Huffman et al., 1995] (Fig 4). The precipitation estimates from the TRMM data show distinctive peaks at two latitudinal ranges, $18^\circ N - 22^\circ N$ and $27^\circ N - 32^\circ N$. The high precipitation rate and small precipitation fraction suggests episodic intensive rain events at $18^\circ N - 22^\circ N$ whereas the high precipitation rate and high precipitation fraction suggests frequent intensive rain events at $27^\circ N - 32^\circ N$. The simulation results show similar intensive rain events at $27^\circ N - 32^\circ N$. Additionally the simulation results show episodic rain events (high intensity in limited areas) at $32^\circ N - 37^\circ N$. The simulated precipitation is by a factor of 5 lower than derived. This may be due to the limitations of the micrometeorology representation in the model, which could allow occasional growth of rain drops.

4.2. In-cloud production of sulfate

4.2.1. A case study for DC8 Flt.14 and P3B Flt.16.

On March 24, 2001 two aircraft flights were conducted in the southeast of Japan and across the Honshu island, Japan by DC-8 Flt.14 and P-3B Flt.16, respectively. Fig 5(a) and (b) show the satellite GMS-5 visible channel images taken at 3:23Z March 24, which is close to the halfway of these flights in time, superimposed by these two flight tracks (DC-8 Flt. 14 and P-3B Flt.16 flight tracks in Fig 5(a) and (b), respectively). These two satellite images depict deep convective activity extending from further west of $120^\circ E$ to $140^\circ E$, sparse convective clouds between $140^\circ E$ and $145^\circ E$, and a moderately convective cloud band further east of $145^\circ E$ in the south of the Japan islands. The convective clouds were observed to have formed over the eastern China on the previous day and developed eastward to $140^\circ E$ by the time of the flights. This is one of a few intensive

thunderstorms observed in the vicinity of the in-situ measurements during TRACE-P. The flight tracks superimposed on the satellite images show both flights partly intercepted the cloudy regions to the south of Japan islands and successfully sampled cloud-influenced air. Fig 6 shows the predicted distributions of column sulfate (colored) and cloud water (liquid+ice) path in excess of $1g/m^2$ (an area confined with a white bold dashed line and filled with white crosses) for 0Z March 24. The two boxes indicated by a black solid line in Fig 6 show the positions of the satellite images in Fig 5 (the smaller box for Fig 5(a) and the larger box for Fig 5(b)). The sulfate released into air after being produced via in-cloud processing is derived by subtracting $S(VI)_{trc}$ from $S(VI)_a$. The distribution of vertically integrated amounts of this sulfate is shown with contours in Fig 6. The simulated cloud fields are found over the eastern part of China to $135^\circ E$ within the latitudinal ranges between $25^\circ N$ and $35^\circ N$ and in the east of $140^\circ E$ between $30^\circ N$ and $40^\circ N$, which are in good agreement with those in the satellite images except for the slight displacement of the northeastern portion of the clouds toward the north in the prediction. The model results show the significant amount of sulfate off the coast of China extending across the East China Sea. The significantly high amounts of sulfate (1 ppbv - 4.2 ppbv) that has been released into air after produced via in-cloud processing are seen where the deep convective activity is observed (centered at $30^\circ N$, $125^\circ E$). The second peak of this sulfate is seen in the east of the main peak at around $33^\circ N$ and $142^\circ E$. Fig 7(a) is a contour plot of the vertical cross section of the simulated sulfate ($S(VI)_a$) along the flight track of DC-8 Flt.14. The altitude of the aircraft is indicated by a dotted line. The visible aerosol scattering ratio measured using UV DIAL (Differential Absorption Lidar) system on DC-8 reveals the vertical profile of aerosols for this flight (not shown)

[Browell, 2003]. It shows high aerosol levels throughout the boundary layer, a relatively high aerosol level at the altitude of 6km at between 8.8×10^4 and 9.0×10^4 sec (UTC), and an elevated level of an aerosol layer at about 7km at between $1.10 \times 10^5 - 1.14 \times 10^5$ sec (UTC). The good agreement between the simulated sulfate vertical profile and the vertical profile of the visible aerosol scattering ratio suggests that the model qualitatively captures the sulfate vertical distribution for this flight. Fig 7(b) and (c) show the sulfate ($S(VI)_a$) mixing ratio and relative humidity of simulated (bold solid line) and measured (dotted line) at the same vertical slice as in Fig 7(a). Fig 8(a)-(c) show corresponding data along the P-3B Flt.16 flight track. Considerably elevated sulfate mixing ratios (1 ppbv - 5 ppbv) were observed in the both flights as denoted A - G in Fig 7(b) and 8(b). The geolocations of these peaks are shown in Fig 6. All of the peaks are observed in the boundary layer except for the peak D and F, which are observed at the altitude of 1.5km. The high relative humidity (90 - 100%) measured (Fig 7(c)) at B and satellite image (Fig 5(a)) indicate the air sampled within the cloud. The mixing ratios at C, E and G are probably near the cloud edge or outside the cloud since the relative humidity is moderately high ($\sim 80\%$) but not as high as that found within clouds. The comparisons of the sulfate mixing ratios between the simulation and the measurements show an excellent agreement in the background sulfate mixing ratios. The simulated sulfate mixing ratios at B - G are much smaller than those of the measured while that at A is twice higher than that measured. The SO_2 mixing ratio at E is considerably underestimated in the simulation, and consequently the sulfate mixing ratio is underestimated. The model misses capturing the peaks at D and F, which are observed at the altitude of 1.5km. In addition to the $S(VI)_a$ mixing ratios, $S(VI)_{trc}$ mixing ratios, which are not subject to in-cloud

processing, are plotted in Fig 7(b) and Fig 8(b). Comparing the $S(VI)_a$ mixing ratios with the $S(VI)_{trc}$ mixing ratios, there is a significant enhancement of $S(VI)_a$ at B, C, E, and G. Considering the relative humidity of 90% – 100% at B, the enhancement of sulfate is due to in-cloud processing. The sulfate at C, E and G is also produced in clouds that have evaporated by the time of the measurements. There is little enhancement in sulfate mixing ratios from $S(VI)_{trc}$ at A, therefore the sulfate is suggested to be produced other than in-cloud processing.

4.2.2. Net sulfate production.

The sulfate produced via in-cloud processing in the East Asian region for March 7 - April 3, 2003 is now estimated by integrating the total sulfate within the regional domain. The sulfate produced via in-cloud processing may be released into air, remain in clouds, or be lost through precipitation. Fig 9(a) shows time series of the volume integrated $S(VI)_a$ and $S(VI)_{trc}$ mass. The difference (Fig 9(b)) between these two curves reflects the volume integrated sulfate mass that is released into air after being produced in clouds. Fig 9(c) shows the sulfate mass remaining in clouds (the volume integrated $S(VI)_t$ mass indicated by a solid line) and the sulfate mass lost through precipitation (dotted line). The sulfate mass released into air after being produced in clouds varies in the ranges between $1.5 \times 10^6 kg$ and $7.5 \times 10^6 kg$, remaining in clouds is $0.2 \times 10^6 kg - 3.5 \times 10^6 kg$, and being precipitated is $0.01 \times 10^6 kg - 1.8 \times 10^6 kg$. The fate of sulfate in clouds is determined by the microphysical properties of the cloud and the local meteorological conditions. If the cloud is non-precipitating, then the sulfate in the cloud remains in the atmosphere or is removed through dry deposition, which is not an effective pathway of sulfate removal [Davis et al., 2003]. If the cloud produces rain, the sulfate may be lost

through rain out (acid rain). As mentioned in the previous section, the intensive deep convective activity was observed on March 24. During this episode, the model predicts that a large amount of sulfate was produced in clouds and released into air as the cloud evaporated. The time series in Fig 9(b) clearly indicates this event as a peak between 24th and 26th. Sulfate remaining inside the clouds rapidly increases at the beginning of the convective period (March 23), and decreases as the clouds evaporate (late March 23) (solid line in Fig 9(c)). The curve of sulfate precipitated (dotted line in Fig 9(c)) indicates the storm on March 24 did not produce particularly severe acid rain since the large portion of sulfate produced in clouds may have been released into air. In contrast to the storm on March 24, the model predicts that the clouds formed between March 15th and 16th do not release a large amount of sulfate into air. Instead, a large portion of sulfate is precipitated. Fig 9(d) shows the sum of the sulfate mass suspended in air ($S(VI)_a$) and that in clouds ($S(VI)_t$) as a local sulfate source (solid line), and also the sulfate mass lost through precipitation as a local sulfate sink (dotted line). Throughout the simulation the total sulfate source exceeds the sink by far. This is compared with the global sulfate sources and sinks. Davis et al. [2003] shows the global sources and sinks of sulfate obtained from seven global sulfur model runs. The median value of the sulfate source due to in-cloud processing obtained from these global models is 40.0 Tg S/yr whereas the median value of the sulfate sink due to wet deposition is 44.5 Tg S/yr. According to these results, the global sulfate loss due to wet deposition exceeds the global source due to in-cloud processing by 4.5 Tg S/yr. Fig 9(d) shows that in the East Asian region the sulfate source due to in-cloud processing is much larger than the sink due to wet deposition, and therefore contribution to a net sulfate input to the atmosphere. The

comparisons of the simulated cloud and precipitation fields with the satellite retrieved values have shown the considerable underestimates of cloud and precipitation fractions in the simulation. The underestimate of cloud fraction introduces negative bias to sulfate mass produced in clouds (the source) while the underestimate of precipitation fraction introduces negative bias to sulfate mass precipitated (the sink). Assessing the impact of these biases on the sulfate budget is beyond the scope of this study.

Fig 10(a) and (b) are the zonal average of $S(VI)_a$ and $S(VI)_{trc}$ mixing ratios, respectively, between $15^\circ N$ and $50^\circ N$ for March 7 to April 3, 2001. Both show high mixing ratios ($1.65ppbv$ for $S(VI)_a$ and $1.35ppbv$ for $S(VI)_{trc}$) at $24^\circ N$ - $29^\circ N$. The difference between these two distributions, which accounts for the sulfate mixing ratio released into air after produced in clouds, is shown in Fig 10(c). This shows that sulfate is released from clouds into the atmosphere below 1km. The maximum difference ($0.15ppbv$) between $S(VI)_a$ and $S(VI)_{trc}$ is seen at around $30^\circ N$ while the maximum cloud liquid water mixing ratio is found at $26^\circ N$ (Fig 10(d)). The possible cause of this difference is that amounts of H_2O_2 available for the oxidation is small relative to liquid water amounts at about $30^\circ N$ and thus limits the conversion of SO_2 to sulfate.

5. Summary and conclusions

The objective of this study was to estimate the contribution of the sulfate in-cloud production to the total sulfate in East Asia during the TRACE-P period. A regional simulation of the sulfate transport for the TRACE-P period was conducted using UWNMS with an aqueous sulfur chemistry model. First, the model performance in predicting distributions of SO_2 , sulfate, H_2O_2 , liquid cloud water and precipitation was assessed by comparing with in-situ measurements and satellite observations. The comparisons

revealed the overestimated by 20% between $1\text{km} - 6\text{km}$ and the underestimates by 30% near the surface and by 50% above 6km . The predictions were overestimated SO_2 and H_2O_2 mixing ratios by a factor of $1.2 - 3$ at almost all altitude and latitude bins. Despite these discrepancies, the relative patterns of their vertical and latitudinal variations were in good agreement with in-situ measurements. The comparisons of liquid water path between the simulation and the satellite observation show that the simulated cloud frequencies were low. The precipitation rates are by a factor of 5 smaller than those derived based on the TRMM data. This possibly altered the sulfate budget in the lower troposphere.

A case study was conducted for March 24, 2001, when air influenced by a deep convective storm was advected from the east coast of China to the south of Japan islands. The regional simulation identified the enhancement of sulfate due to in-cloud processing by comparing the standard sulfate mixing ratios with the idealized sulfate tracer mixing ratios. However, it underestimated the mixing ratios of sulfate that was released in air by a factor of 2.

Volume integrated sulfate mass in the regional domain was calculated during the TRACE-P period. The total sulfate mass varied between $4.25 \times 10^7\text{kg}$ and $6.4 \times 10^7\text{kg}$ due to transport, in-cloud production and removal through precipitation. Instantaneous sulfate mass of $2 \times 10^6\text{kg} - 3.5 \times 10^6\text{kg}$ was predicted in clouds. The fate of this in-cloud sulfate is determined by the microphysical properties of the cloud and the local meteorological conditions. This study showed that the sulfate input to the atmosphere exceeds the sulfate removed from the atmosphere through precipitation in the East Asian region during the TRACE-P. Consequently, East Asia in spring can be an important source region of sulfate and thus offset the sulfate loss in other regions of the globe. This should

not be extrapolated to other seasons since the East Asian region in spring has more favorable conditions for sulfate in-cloud production than other regions of the globe. The quantification of the sulfate input in East Asia requires accurate predictions of meteorological variables. Therefore errors in the predicted clouds and precipitation can result in a significant impact on the sulfate budget.

Acknowledgments.

Support for this work was provided by the NASA Atmospheric Chemistry Modeling and Analysis Program (ACMAP) and the NASA Langley Research Center (LaRC) Creativity and Innovation Program. Brian Heikes, Daniel O’Sullivan and Julie Snow are thanked for sharing their hydrogen peroxide. One of the authors (C. Kittaka) thanks T. D. Fairlie for his comments and suggestions in preparing this manuscript.

References

- Borys, R. D., E. E. Hindman, and P. J. Demott, The chemical fractionation of atmospheric aerosol as a result of snow crystal formation and growth, *J. Atmos. Chem.*, *7*, 213–239, 1988.
- Browell, E. V., et al., Large-scale ozone and aerosol distributions, air mass characteristics, and ozone fluxes over the western Pacific Ocean in late winter/early spring, *J. Geophys. Res.*, *108*(D20), 8805, doi:10.1029/2002JD003290, 2003.
- Calvert, J. G., et al., Chemical mechanisms of acid generation in the troposphere, *Nature*, *317*, 27–35, 1985.
- Carmichael, G., et al., Regional-scale chemical transport modeling in support of intensive field experiments: Overview and analysis of the TRACE-P observations, *J. Geophys.*

- Res.*, 180(D21), 8823, doi:10.1029/2002JD003117, in press, 2003.
- Chin, M., R. B. Rood, S.-J. Lin, J.-F. Müller, and A. M. Thompson, Atmospheric sulfur cycle simulated in the global model GOCART: Model description and global properties, *J. Geophys. Res.*, 105, 24,671–24,687, 2000a.
- Chin, M., et al., Atmospheric sulfur cycle simulated in the global model GOCART: Comparison with field observations and regional budgets, *J. Geophys. Res.*, 105, 24,689–24,712, 2000b.
- Chin, M., et al., Tropospheric aerosol optical thickness from the GOCART model and comparisons with satellite and sun photometer measurements, *J. Atmos. Sci.*, 59, 461–483, 2002.
- Chin, M., et al., A global aerosol model forecast for the ACE-Asia field experiment, *J. Geophys. Res.*, 108(D23), 8654, doi:10.1029/2003JD003642, 2003.
- Crawford, J., et al., Clouds and trace gas distributions during TRACE-P, *J. Geophys. Res.*, 108(D21), 8818, doi:10.1029/2002JD003177, in press, 2003.
- Diehl, K., Mitra, S. K., Pruppacher, H. R., A laboratory study on the uptake of HCl , HNO_3 , and SO_2 gas by ice crystals and the effect of these gases on the evaporation rate of the crystals, *Atmos. Environ.*, 47-48, 235–244, 1998.
- Dibb, J. E., R. W. Talbot, E. Scheuer, G. Seid, M. A. Avery, and H. B. Singh, Aerosol chemical composition in Asian Continental outflow during TRACE-P: Comparison to PEM-West B, *J. Geophys. Res.*, 108(D21), 8815, doi:10.1029/2002JD003111, in press, 2003.
- Dickerson, R. R., Thunderstorms: an important mechanism in the transport of air pollutants, *Science*, 235, 460–465, 1987.

- Eisele, F. L., et al., Summary of measurement intercomparisons during TRACE-P, *J. Geophys. Res.*, *108*(D20), 8791, doi:10.1029/2002JD003167, 2003.
- Hitchman, M. H., M. L. Buker, R. D. Torn, G. J. Tripoli, R. B. Pierce, and J. A. Al-Saadi, A modeling study of an East Asian convective complex during March 2001, *J. Geophys. Res.*, this issue.
- Hoppel, W. A., and G. M. Frick, Submicron aerosol size distributions measured over the tropical and South Pacific, *Atmos. Environ.*, *24A*, 645–669, 1990.
- Huffman, G. J., R. F. Adler, B. Rudolf, U. Schneider, and P. R. Keehn, Global precipitation estimates based on a technique for combining satellite-based estimates, rain gauge analysis, and NWP model precipitation information, *J. Climate*, *8*, 1284–1295, 1995.
- IPCC 2001, Climate Change 2001: The Scientific Basis, J. T. Houghton et al. (eds), Cambridge University Press, UK, 2001.
- Jacob, D. J., et al., The Transport and Chemical Evolution over the Pacific (TRACE-P) mission: Design, execution and overview of results, *J. Geophys. Res.*, *108*(D20), 8781, doi:10.1029/2002/JD003276, 2003.
- Jaeglé, L., et al., Sources and budgets for CO and O_3 in the Northeastern Pacific during the spring of 2001: Results from the PHOBEA-II Experiments, *J. Geophys. Res.*, *108*(D20), 8802, doi:10.1029/2002JD003121, 2003.
- Kiley, C. M., et al., An intercomparison and evaluation of aircraft-derived and simulated CO from seven chemical transport models during the TRACE-P experiment, *J. Geophys. Res.*, *108*(D21), 8819, doi:10.1029/2002JD003089, in press, 2003.
- Kittaka, C., A modeling study of transport and transformation of sulfur species in a deep convective cloud, Ph.D. thesis, Univ. of Wisconsin-Madison, WI, 2001.

- Kreidenweis, S. M., Y. Zhang, and G. R. Taylor, The effects of clouds on aerosol and chemical species production and distribution, 2. Chemistry model description and sensitivity analysis, *J. Geophys. Res.*, *102*, 23,867–23,882, 1997.
- Mitchell, D. L., and D. Lamb, Influence of riming on the chemical composition of snow in winter orographic snow, *J. Geophys. Res.*, *94*, 14,831–14840, 1989.
- Pickering, K. E., et al., Convective transport of biomass burning emissions over Brazil during TRACE-A, *J. Geophys. Res.*, *101*, 23,993–24,012, 1996.
- Pierce, R. B., et al., Regional Air Quality Modeling System (RAQMS) predictions of the tropospheric ozone budget over East Asia, *J. Geophys. Res.*, *108*(D21), 8825, doi:10.1029/2002JD003176, in press, 2003.
- Davis, D. D., G. Chen, and M. Chin, Atmospheric Sulfur, in *Handbook of Weather, Climate, and Water: Atmospheric Chemistry, Hydrology, and Societal Impacts*, edited by T. D. Potter and B. R. Colman, John Wiley & Sons, Inc., New Jersey, 2003.
- Price H. U., D. A. Jaffe, P. V. Doskey, I. McKendry, and T. L. Anderson, Vertical profiles of O_3 , aerosols, CO and $NMHC$ s in the Northeast Pacific during the TRACE-P and ACE-ASIA experiments, *J. Geophys. Res.*, *108*(D20), 8799, doi:10.1029/2002JD002930, 2003.
- Schwartz, S. E., Mass-transport limitation to the rate of in-cloud oxidation of SO_2 : Re-examination in the light of new data, *Atmos. Environ.*, *22*, 2491–2499, 1988.
- Seinfeld, J. H., and S. N. Pandis, *Atmospheric Chemistry and Physics*, 1326 pp, Wiley-Interscience, New York, 1998.
- Streets, D. G., et al., An inventory of gaseous and primary aerosol emissions in Asia in the year 2000, *J. Geophys. Res.*, *108*(D21), 8809, doi:10.1029/2002JD003093, in press,

2003.

Tripoli, G. J., A nonhydrostatic numerical model designed to simulate scale interaction, *Mon. Wea. Rev.*, *120*, 1342–1359, 1992.

Tu F.-H., et al., Dynamics and transport of sulfur dioxide over the Yellow Sea during TRACE-P, *J. Geophys. Res.*, *108*(D20), 8790, doi:10.1029/2002JD003227, 2003.

Weber, R. J., et al., New particle Formation in Anthropogenic Plumes Advecting from Asia Observed During TRACE-P, *J. Geophys. Res.*, *108*(D21), 8814, doi:10.1029/2002JD003112, in press, 2003.

Figure 1. Altitude binned results of model predictions and in-situ measurements characterized by their median (vertical line), 50 percentile (box) and 90 percentiles (horizontal lines): a) SO_2 , b) sulfate and c) H_2O_2 .

Figure 2. Same as Fig 1 except the mixing ratios are sorted into six different latitudinal bins.

Figure 3. a) Latitudinal variations of liquid water path (g/m^2) calculated from the UWNMS results (solid) and the MODIS data (dashed). The median and 90 percentiles are determined from liquid water path of more than $20g/m^2$ at each latitudinal bin and b) latitudinal variations of liquid water ($> 20g/m^2$) fraction (%).

Figure 4. a) Latitudinal variations of precipitation rate (mm/d) calculated from the UWNMS results (solid) and derived based on the TRMM data (dashed). The median and 90 percentiles are determined from precipitation rate of more than $0.1mm/d$ and b) latitudinal variations of precipitation ($> 0.1mm/d$) fraction (%).

Figure 5. The satellite GMS-5 visible channel images at 3:23Z March 24 superimposed by a) DC-8 Flt.14 and b) P-3B Flt.16 flight tracks.

Figure 6. Vertically integrated sulfate $S(VI)_a$ (colored), sulfate produced via in-cloud processing (solid contours with a contour interval of $1 \times 10^{15} molec/cm^2$), liquid water mixing ratio of $0.1 g/kg$ (dashed line) for 06Z March 24, 2001 and flight tracks (DC8 Flt.14: black, P3B Flt.16: gray).

Figure 7. a) Vertical cross section of sulfate $S(VI)_a$ (solid contours) along the DC8 Flt.14 flight track (the flight altitude is indicated by a dotted line). The contour interval is 0.2 ppbv, b) time series of sulfate mixing ratios along the flight track (predicted $S(VI)_a$: bold solid, predicted $S(VI)_{trc}$: solid, measured: dashed), and c) time series of relative humidity along the flight track (predicted: solid, measured: dashed).

Figure 8. Same as Fig 7 except for P3B Flt.16.

Figure 9. a) Time series of the volume integrated sulfate ($S(VI)_a$) mass in the regional domain (solid) and the volume integrated idealized sulfate tracer ($S(VI)_{trc}$) mass (dashed), b) the difference between two curves in a), c) instantaneous sulfate mass contained in clouds $S(VI)_t$ (solid) and sulfate mass lost through rain out (dashed) and d) the sum of the volume integrated masses of $S(VI)_a$ and $S(VI)_t$ (solid), and the sulfate mass lost through rain out (dashed).

Figure 10. a) Zonal averaged mixing ratios of $S(VI)_a$, b) zonal average mixing ratios of the idealized sulfate tracer $S(VI)_{trc}$, c) the differences between a) and b), and d) zonal averaged cloud mixing ratios (liquid water: solid, ice: dashed).

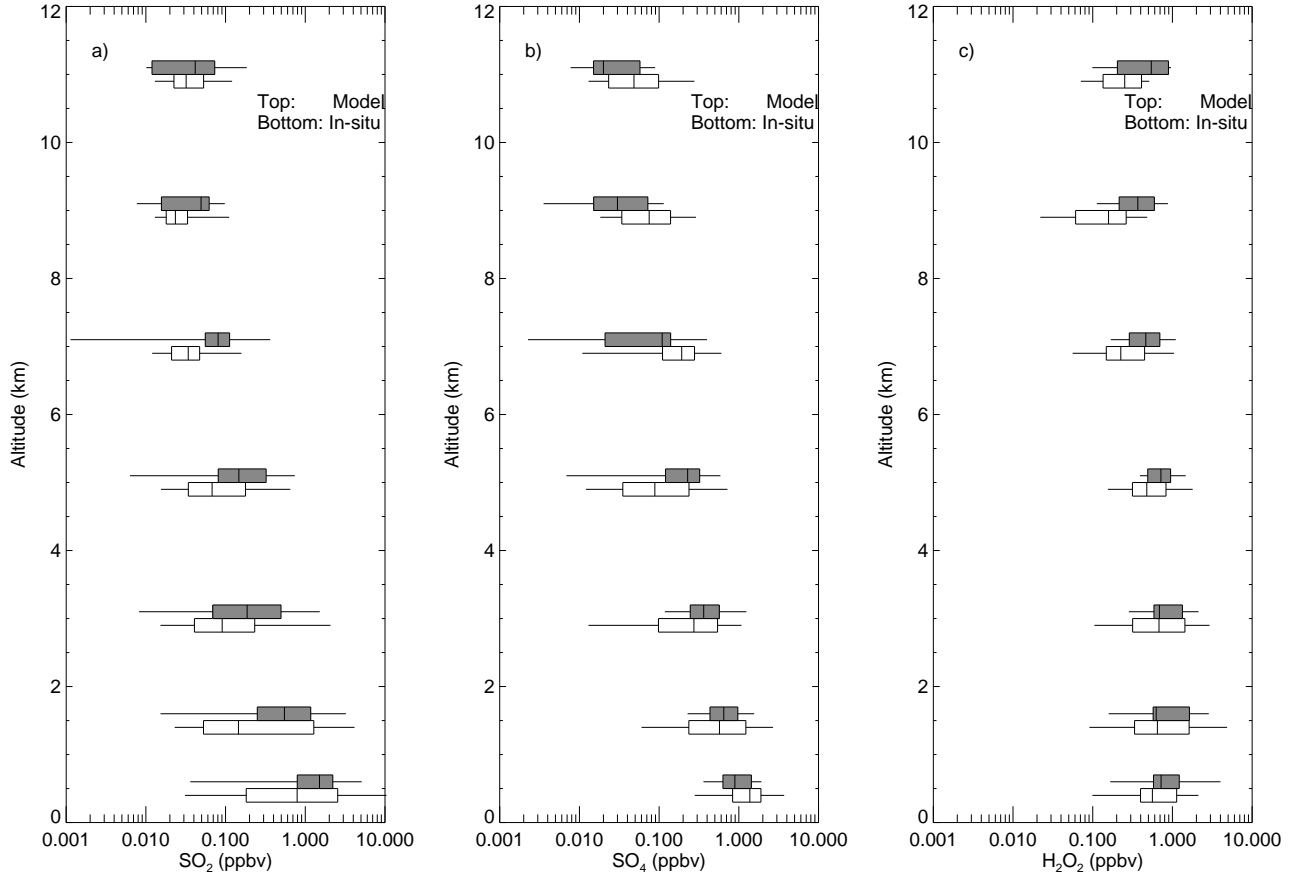


Figure 1. Altitude binned results of model predictions and in-situ measurements characterized by their median (vertical line), 50 percentile (box) and 90 percentiles (horizontal lines): a) SO_2 , b) sulfate and c) H_2O_2 .

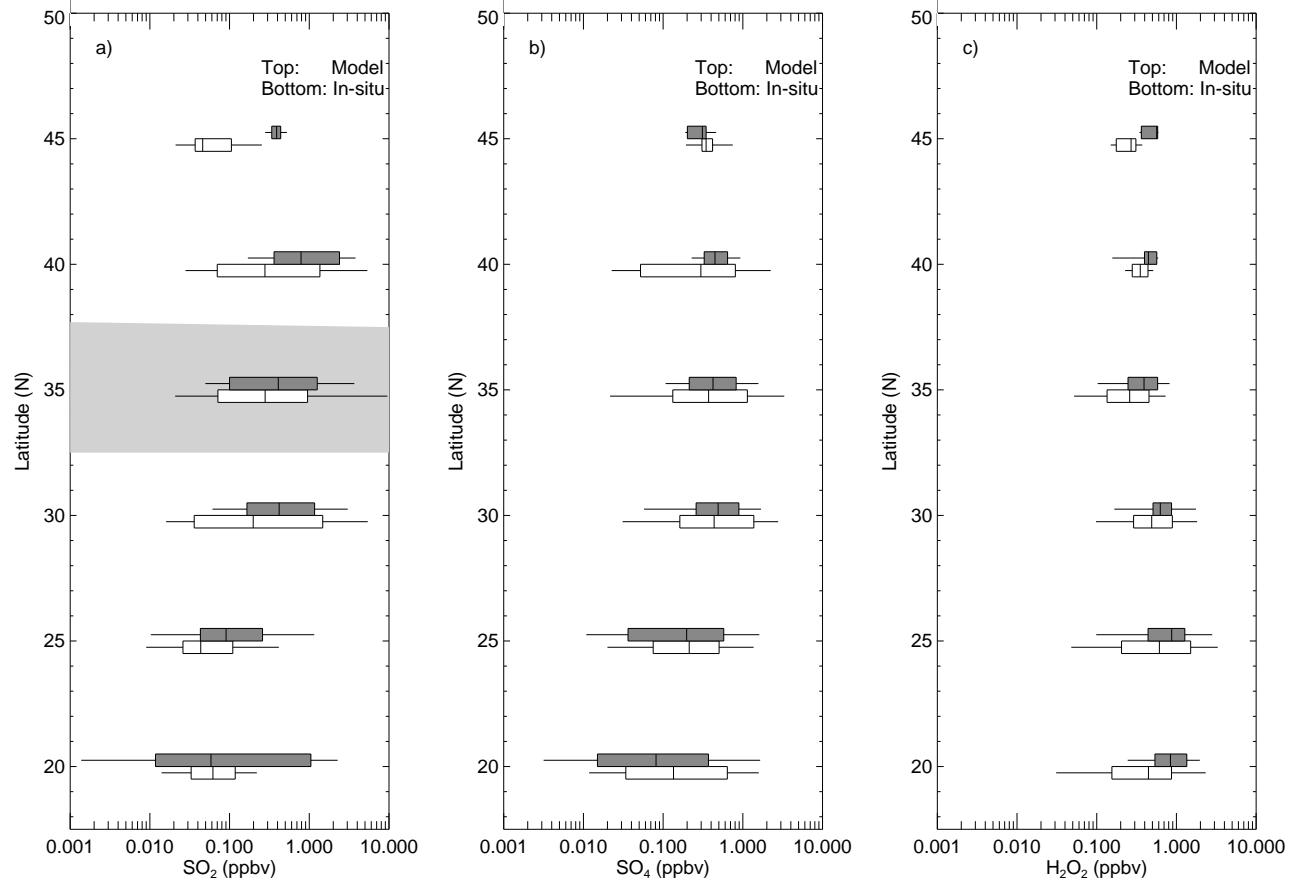


Figure 2. Same as Fig 1 except the mixing ratios are sorted into six different latitudinal bins.

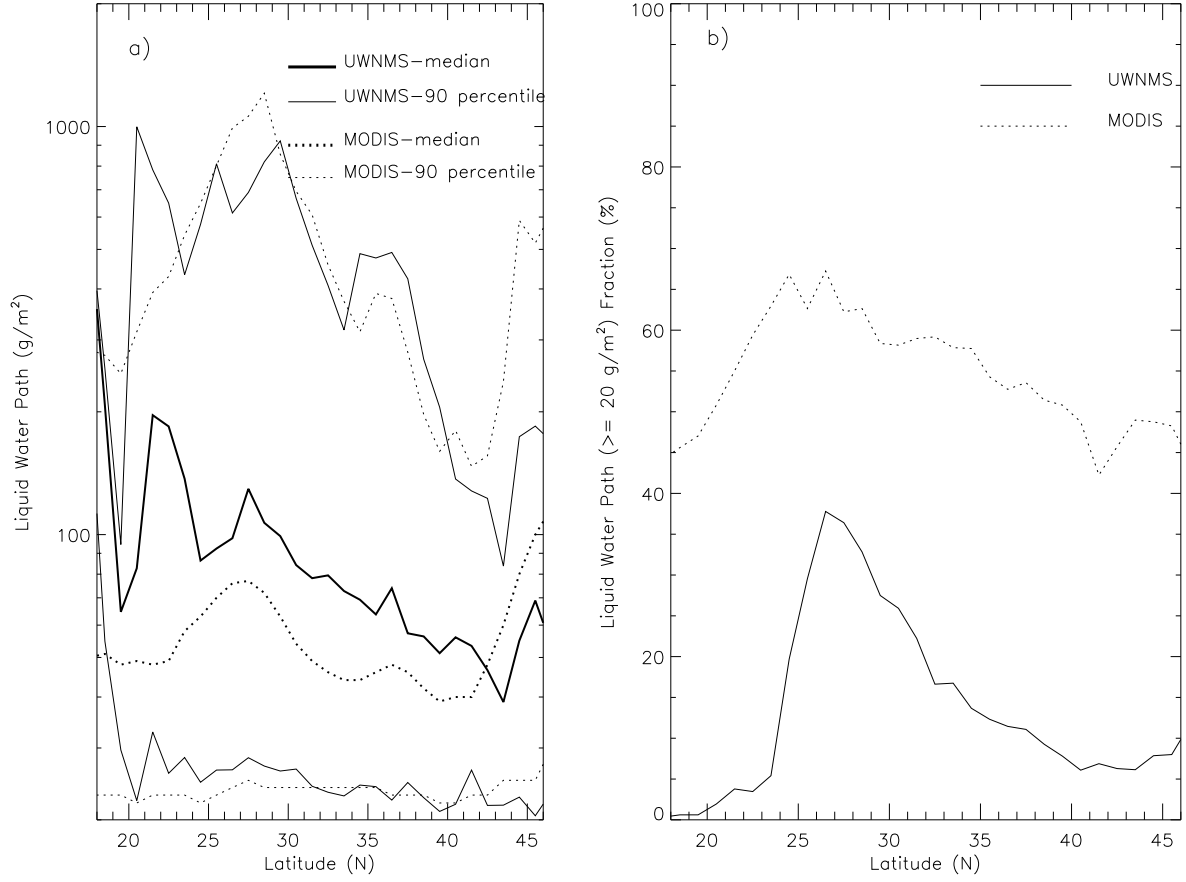


Figure 3. a) Latitudinal variations of liquid water path (g/m^2) calculated from the UWNMS results (solid) and the MODIS data (dashed). The median and 90 percentiles are determined from liquid water path of more than $20 \text{ g}/\text{m}^2$ at each latitudinal bin and b) latitudinal variations of liquid water ($> 20 \text{ g}/\text{m}^2$) fraction (%).

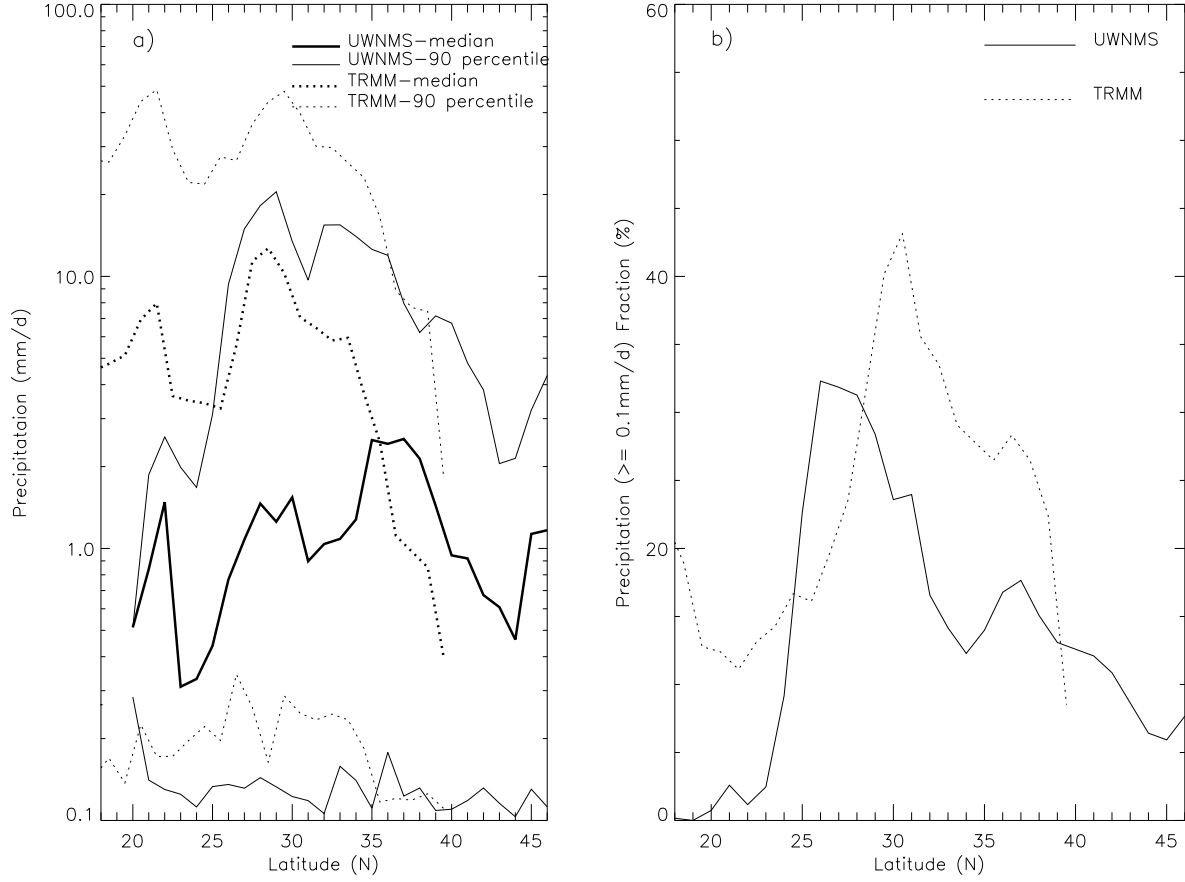


Figure 4. a) Latitudinal variations of precipitation rate (mm/d) calculated from the UWNMS results (solid) and derived based on the TRMM data (dashed). The median and 90 percentiles are determined from precipitation rate of more than $0.1mm/d$ and b) latitudinal variations of precipitation ($> 0.1mm/d$) fraction (%).

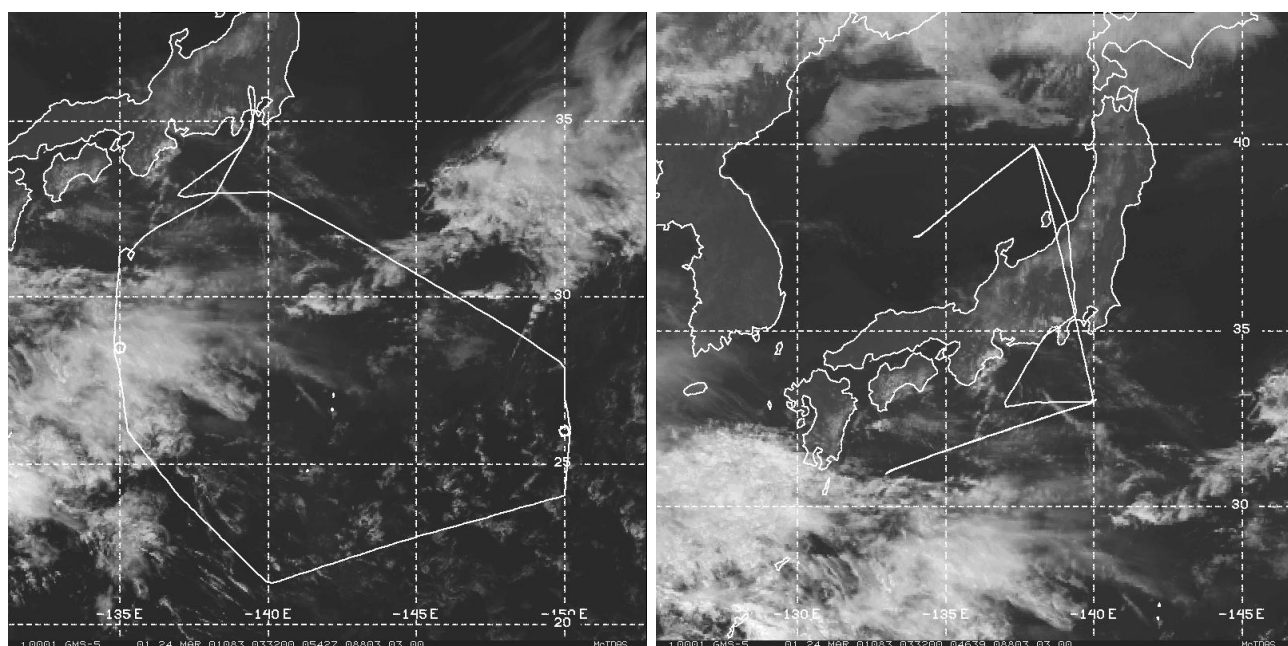


Figure 5. The satellite GMS-5 visible channel images at 3:23Z March 24 superimposed by a) DC-8 Flt.14 and b) P-3B Flt.16 flight tracks.

Predicted Sulfate Distribution at 06Z March 24, 2001

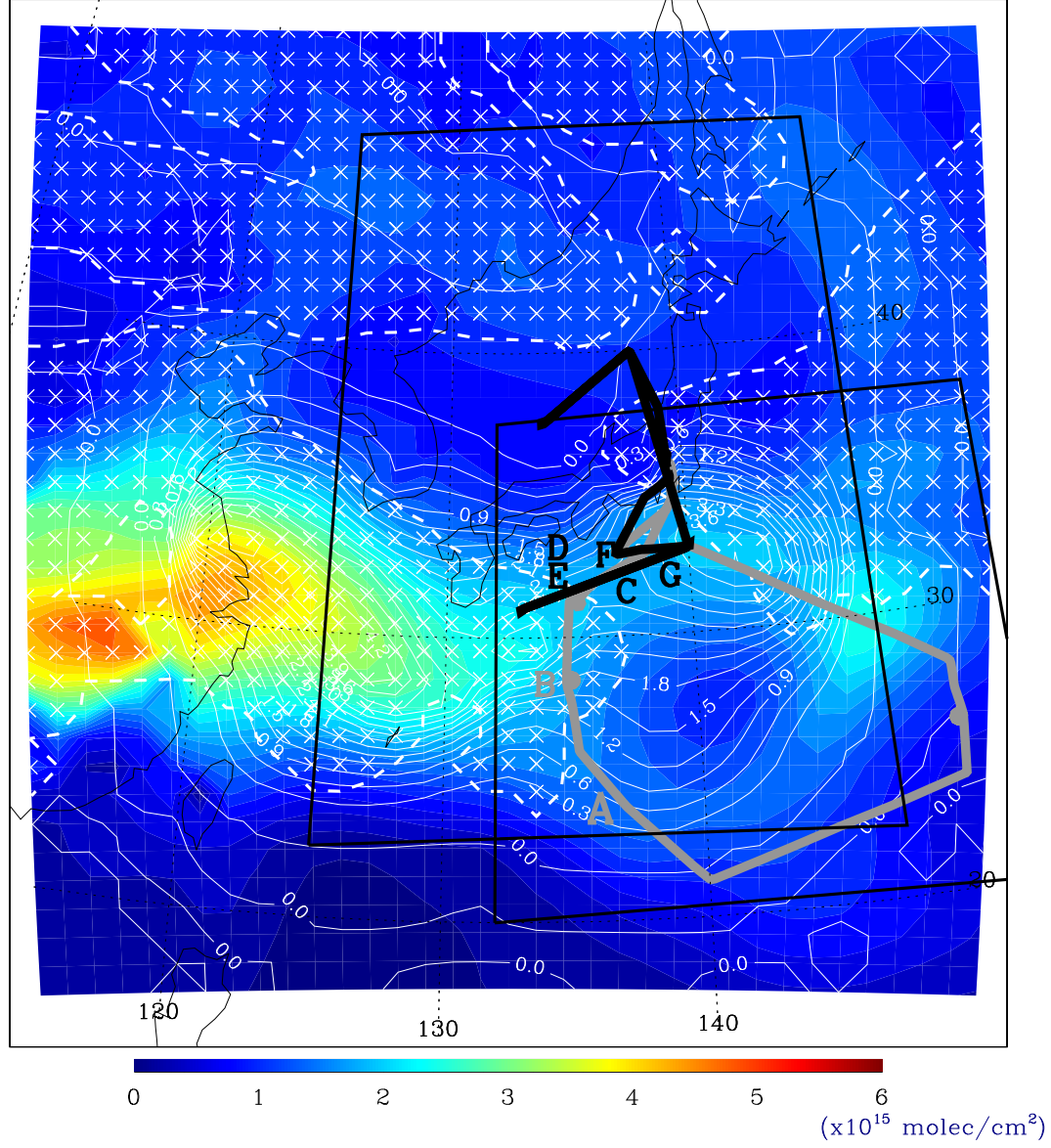


Figure 6. Vertically integrated sulfate $S(VI)_a$ (colored), sulfate produced via in-cloud processing (solid contours with a contour interval of $1 \times 10^{15} \text{ molec/cm}^2$), liquid water mixing ratio of 0.1 g/kg (dashed line) for 06Z March 24, 2001 and flight tracks (DC8 Flt.14: black, P3B Flt.16: gray).

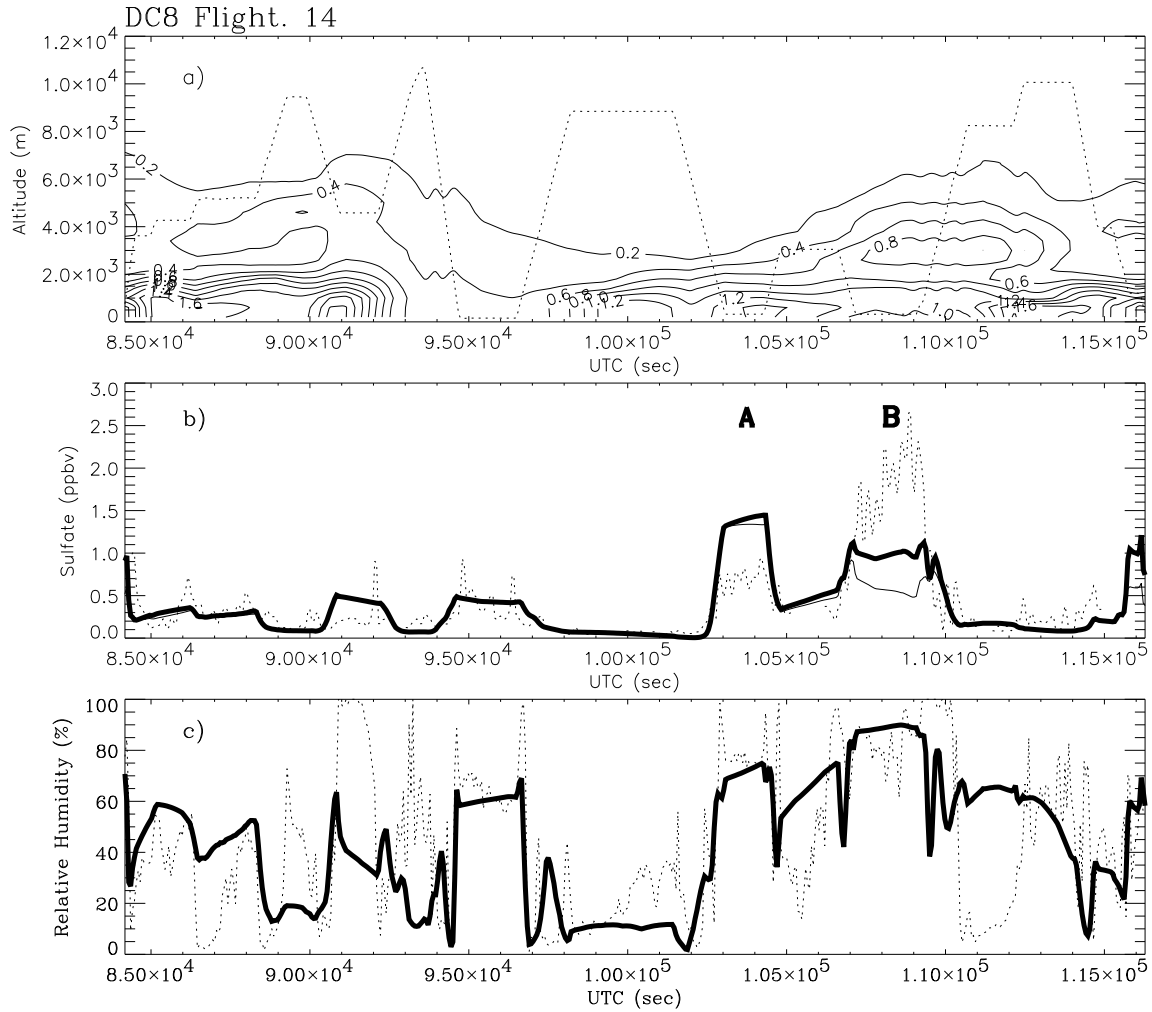


Figure 7. a) Vertical cross section of sulfate $S(VI)_a$ (solid contours) along the DC8 Flt.14 flight track (the flight altitude is indicated by a dotted line). The contour interval is 0.2 ppbv, b) time series of sulfate mixing ratios along the flight track (predicted $S(VI)_a$: bold solid, predicted $S(VI)_{trc}$: solid, measured: dashed), and c) time series of relative humidity along the flight track (predicted: solid, measured: dashed).

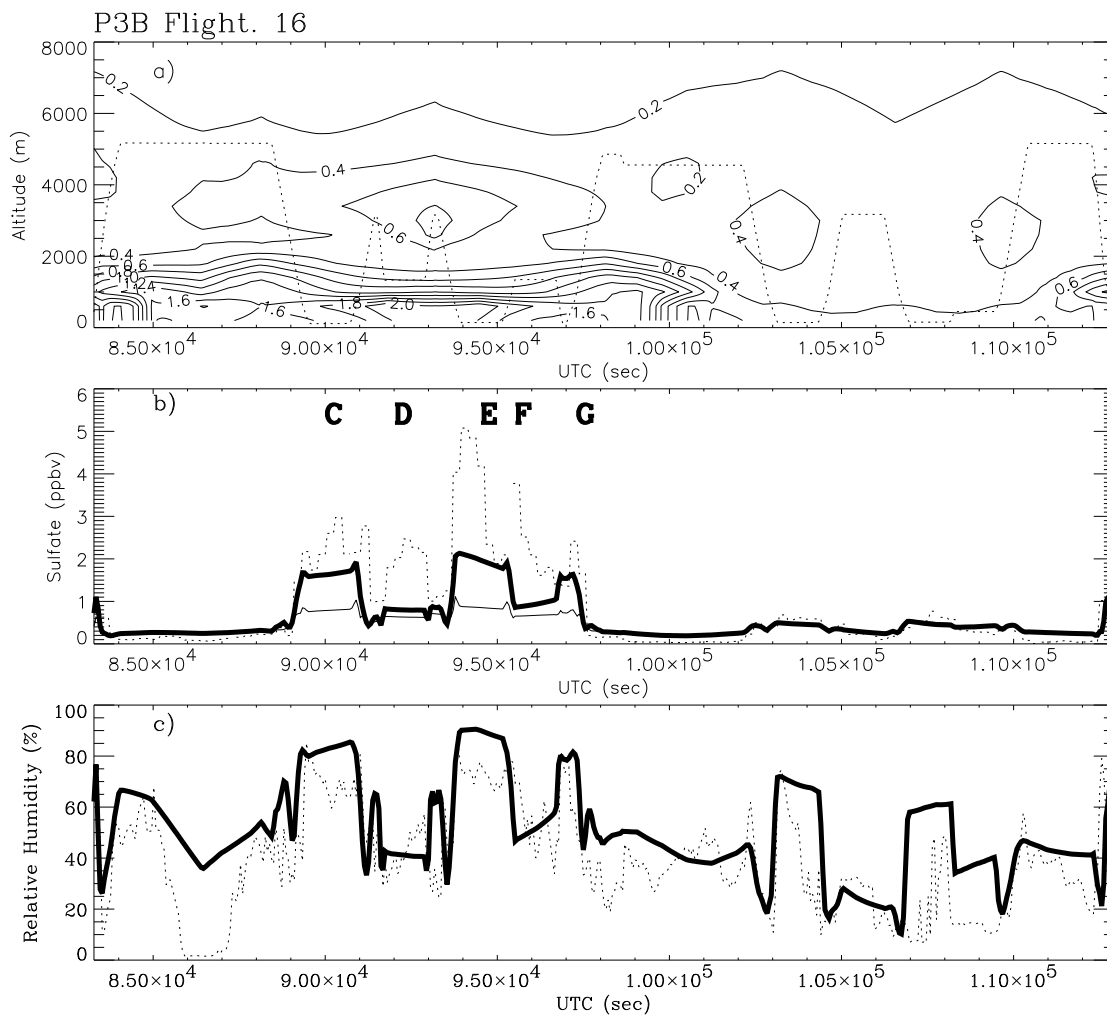


Figure 8. Same as Fig 7 except for P3B Flt.16.

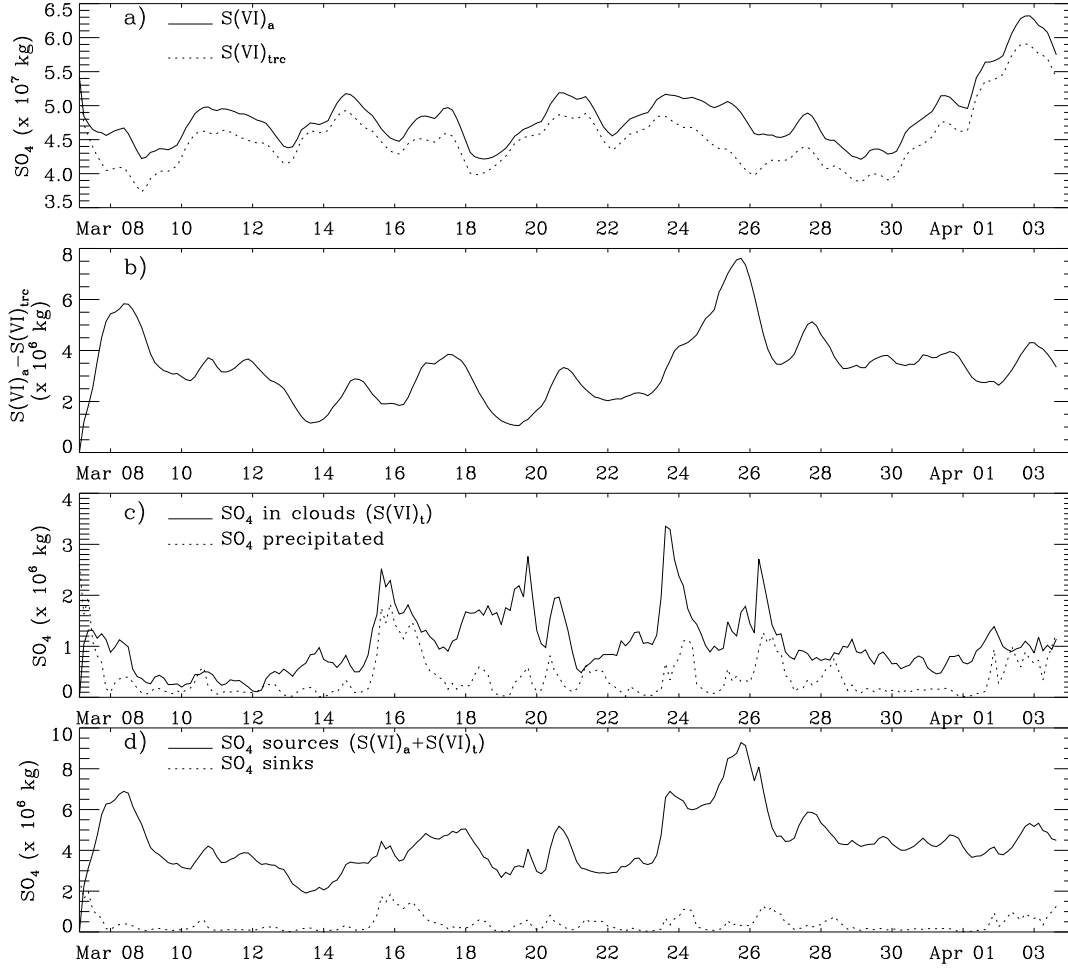


Figure 9. a) Time series of the volume integrated sulfate ($S(VI)_a$) mass in the regional domain (solid) and the volume integrated idealized sulfate tracer ($S(VI)_{trc}$) mass (dashed), b) the difference between two curves in a), c) instantaneous sulfate mass contained in clouds $S(VI)_t$ (solid) and sulfate mass lost through rain out (dashed) and d) the sum of the volume integrated masses of $S(VI)_a$ and $S(VI)_t$ (solid), and the sulfate mass lost through rain out (dashed).

